Reversal mechanism, switching field distribution, and dipolar frustrations in Co/Pt bit pattern media based on auto-assembled anodic alumina hexagonal nanobump arrays

T. Hauet,[1] L. Piraux,[2] S. K. Srivastava,[2,3] V. A. Antohe,[2] D. Lacour,[1] M. Hehn,[1] F. Montaigne,[1] J. Schwenk,[4] M. A. Marioni,[4] H. J. Hug,[4,5] O. Hovorka,[6] A. Berger,[7] S. Mangin,[1] and F. Abreu Araujo[2]

[1]*Institut Jean Lamour, Université de Lorraine & CNRS, Vandoeuvre lès Nancy, F-54506, France*
[2]*Institute of Condensed Matter and Nanosciences, Université catholique de Louvain, Place Croix du Sud, B-1348, Louvain-la-Neuve, Belgium*
[3]*Amity Institute of Nanotechnology, Amity University, Noida, India-201303*
[4]*Empa, Swiss Federal Laboratories for Materials Science and Technology, CH-8600 Dübendorf, Switzerland*
[5]*Institute of Physics, Universität Basel, CH-4056 Basel, Switzerland*
[6]*Faculty of Engineering and the Environment, University of Southampton, Southampton, SO17 1BJ, UK*
[7]*CIC nanoGUNE Consolider, Tolosa Hiribidea 76, E-20018 Donostia-San Sebastián, Spain*

We fabricated a perpendicularly magnetized bit pattern media using a hexagonally close-packed auto-assembled anodic alumina template with 100 nm and 50 nm periods by depositing a Co/Pt multilayer to form an ordered array of ferromagnetic nanodots, so-called nanobumps. We used Hall resistance measurements and magnetic force microscopy to characterize the dot-by-dot magnetization reversal mechanism under applied field. The role of interdot exchange coupling and dipolar coupling are investigated. Then we focus on separating the various origins of switching field distribution (SFD) in this system, namely dipolar interactions, intrinsic anisotropy distribution, and template packing faults. Finally we discuss the influence of triangular dipolar frustrations on the energy stability of demagnetized and half-switched states based on an Ising model, including local exchange coupling. The impact of SFD and lattice defects lines between misoriented ordered domains on the magnetic configurations is studied in detail.

I. INTRODUCTION

Ordered arrays of isolated magnetic nanostructures are of considerable interest in many fields of fundamental physics as well as in nanotechnology implementations. For the former, artificially frustrated nanomagnets have recently opened new ways of investigating complex phenomena that usually occur in bulk systems such as spin ice with monopolelike excitations [1,2]. Regarding the latter, the best example is probably the research on bit pattern media (BPM), which may lead to improved storage density of hard disks in the near future [3,4]. In both of the above examples, each artificially fabricated magnetic nanostructure is capable of storing one uniform macrospin. Fabrication schemes involve either lithographic patterning [5,6] or a combination of e-beam lithography methods with other techniques such as electrodeposition [7] and self-assembling block copolymers [8]. However, lithographic techniques are expensive and time-consuming. Therefore, it is of interest to develop a nonlithographic patterning method based on self-assembly as an alternative route in order to develop a fast and cheap process capable of producing dense arrays of nanostructures over millimeter-wide areas with precise long-range order. One well-known approach to fabricate BPM is based on self-assembly of colloidal nanospheres [9]. However, several problems associated with the nanosphere technique were pointed out. The presence of dislocations and domains is difficult to prevent. The cleanness and hydrophilic properties of the substrate surface are critical in making well-ordered colloidal crystal films [10]. In addition, attractive forces between the spheres prevent the formation of a layer of spheres with good order when considering diameters below 50 nm so that only short-range order can be obtained or their long-range

order needs to be promoted by templates using lithography [11].

In 2012, we proposed a method for designing low-cost densely packed magnetic particle assemblies on two dimensional (2D) curved substrates with perpendicular magnetic anisotropy (PMA) [12]. This process involves the growth of magnetic nanocaps on the back of nanoporous anodic alumina (AAO) templates, which are a typical self-ordered nanopore-array material formed by the electrochemical oxidation of Al in acidic solutions [13,14]. In our previous report [12], as a proof of concept, we studied a hexagonally close-packed array of [Co/Pt] nanocaps deposited on bumps having about a 100 nm lateral modulation period. We showed that the magnetic hysteresis loops from flat films and bumpy films are very different. Moreover, we observed specific lines of uniformly magnetized bumps after out-of-plane demagnetization that we explained considering dipolar frustration between bumps. We deduced that direct exchange coupling between bumps must be drastically reduced, as described in Ref. [15].

Here we present a study of the magnetization reversal mechanisms of a thin Co/Pt multilayer deposited on a closely packed nanobump array with 100 nm and 50 nm periods. Using extraordinary Hall effect (EHE) and superconducting quantum interference device-vibrating sample magnetometer (SQUID-VSM) measurements, we provide a macroscopic characterization of reversal mechanisms in terms of the switching fields and switching field distribution (SFD) as a function of field angle and temperature. The SFD is quantified in two ways: direct hysteresis loop differentiation and the so-called $\Delta H(M, \Delta M)$ method [16,17]. This method requires as an input the measurement of partial reversal curves and allows the disentanglement of the intrinsic SFD resulting from magnetic and structural inhomogeneity of the bumps from

the effect of dipolar coupling in between the bumps. Then, using magnetic force microscopy (MFM), we demonstrate the bump-by-bump magnetization reversal and hereby reveal the competition between interdot exchange and dipolar couplings. Easy and hard switchers are detected, and their influence on magnetic states during field cycles or after demagnetization is discussed. Finally, we investigated features of AAO lattice stacking faults and their consequences on nanobump arrays in conjunction with their dipolar interactions and SFDs.

II. EXPERIMENTAL DETAILS

A. Sample fabrication and structural features

To obtain ordered arrays of ferromagnetic nanodots, we deposited thin Co/Pt multilayers onto the bumpy barrier-layer surface of AAO templates [12]. The AAO templates were fabricated by a two-step anodization process in order to obtain highly ordered structures [13,14]. The templates with 50 nm and 100 nm average pore spacing consist of long channels ($\sim$50 μm) closed at the bottom end by a round-shaped Al_2O_3 barrier layer [Fig. 1(b)]. The barrier-layer surface self-organizes in a hexagonal close-packed lattice of nanobumps that possesses the same spacing as the porous layer [Figs. 1(a) and 1(c)]. It is used as a prepatterned substrate to modulate the thickness of thin Co/Pt multilayers deposited on it. The multilayers consist of a Ta(5 nm)/Pt(5 nm)/[Co(0.4 nm)/Pt(0.7 nm)]$_4$/Pt(3.5 nm) sequence grown by magnetron sputtering. Due to the bumpy surface, the deposited film experiences a variable thickness along the surface, up to the total thickness of the magnetic stack ($\sim$10 nm) at the top and much thinner close to the bottom of the bumps [15]. In our previous work, it was shown that the magnetic coating of the bumpy surface maintains an out-of-plane magnetic anisotropy, thus forming an ordered
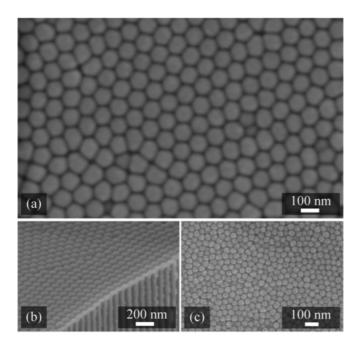

FIG. 1. SEM images of nanobump arrays of a 100 nm period [(a) top and (b) tilted views, respectively] and a 50 nm period [(c) top view].

array of magnetic caps and magnetization pointing up or down perpendicular to the substrate surface [12]. We estimated the mean interbump distance of 105 nm and a full width at half-maximum of 15.5 nm, as described in Ref. [12]. Height modulation profiles extracted from atomic force microscopy (AFM) images show a maximum bump to bump height variation of 5 nm (only 1 nm maximum in region with no lattice defects) and an average bump height distribution of about 2 nm over a few microns, but larger variations (up to 50 nm) can be observed from region to region for areas of tens of microns.

B. Magnetic characterization methods

The extraordinary Hall resistivity measurements were performed by a standard four-probe method. The Hall effect in magnetic materials is commonly described by the phenomenological equation, $\rho_H = R_o H + R_s M_z$, where ρ_H is the Hall resistivity, R_o is the ordinary Hall coefficient, R_s is the extraordinary Hall coefficient, and M_z the component of magnetization perpendicular to the four contacts plane (here perpendicular to the film plane). As in our experiment the ordinary part is much smaller than the extraordinary part, and the extraordinary Hall voltage serves as a direct measurement of magnetization component perpendicular to film plane. Indeed, the hysteresis loop observed in the $\rho_H(H)$ curve was well correlated with the magnetization curve obtained in the same condition of field and temperature using a commercial SQUID-VSM.

Two types of MFM setups have been used for the experiments described here. The first one is a nanoscope AFM/MFM that allows measuring topography and the remanent magnetic configuration at room temperature. The second is a modified nanoscan high-resolution hr-MFM, operated in a vacuum in dynamic mode, whereby the cantilever resonance frequency shifts arising from the tip/sample interaction are recorded and which allows image magnetic configurations in an applied magnetic field. We used a Team-Nanotech hr-MFM-ML1 tip, keeping a tip-sample distance of approximately 8 ± 1 nm on average. Fields were applied using the calibrated permanent magnet driven by the perpendicular field option of the instrument. Prior to the measurements, the tip was separately magnetized in the direction and sense of the field applied during the ramp of field. For each applied field, a stable scan condition was established for the desired tip-sample distance, and the scan was subsequently carried out. In scan series where the sequence of applied magnetic fields included a change of sign, we removed the sample from the field area at zero applied field, flipped the tip magnetization, repositioned the sample, and continued the field sequence. Thus we avoided tip magnetization flip events during the sample magnetization reversal.

The tip is scanned at constant average height corrected for large scale topographical variations of the sample but not for the local topography variations from single bumps. The MFM contrast then arises from changes of the local magnetic stray field, i.e., it reflects the local magnetic state of the sample but also includes contributions of the van der Waals force, which varies with topography-induced changes of the local tip-sample distance. The latter becomes apparent [Fig. 7(a)] in the data recorded at positive saturation (+350 mT). The black dots visible on a gray background reflect the center positions of the

bumps, i.e., a more attractive van der Waals force arising from the smaller tip-sample distance. In order to remove as much as possible of this nonmagnetic contribution to the measured MFM contrast and to focus on the magnetic signal, we use the following procedure. First, we align all images, then we crop them to the area that they all have in common. Subsequently, we subtract from them the image obtained in saturation, which contains essentially the same topographical information as all other images. Finally we center and scale the contrast to ± 1 except in the saturated images.

III. RESULTS AND DISCUSSION

A. Macroscopic features

In Fig. 2(a), the magnetization vs field loops measured by SQUID-VSM at 300 K on the [Co/Pt] stack deposited on flat Si substrate when the field is applied in-plane or out-of plane is presented. This multilayer film shows PMA due to the Co/Pt interfaces [18]. At 300 K, magnetization at saturation is $M_s = 760$ kA/m, and the effective anisotropy field extracted from the in-plane field loop equals $H_k^{\mathrm{eff}} = 470$ mT. These values are in good agreement with previous measurements on similar samples [18]. In Fig. 2(b), the variation of these two parameters is shown as a function of temperature. M_s monotonically increases up to 860 kA/m at 5 K. H_k^{eff} also increases by about 10% at 5 K compared to its room temperature value. At 5 K, H_k^{eff} equals 0.52 T, and the anisotropy constant is 550 kJ/m^3.

The hysteresis loops of a large area specimen made of 100 nm period nanobumps measured by EHE at temperatures ranging from 300 K down to 20 K are shown in Fig. 3(a).
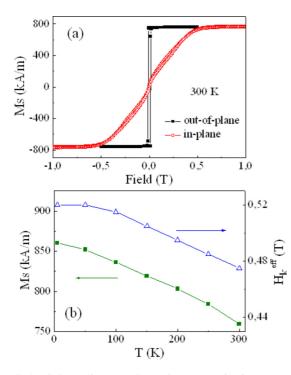

FIG. 3. (Color online) (a) EHE measurements for Co/Pt multilayers on a bumpy surface for $p = 100$ nm measured at 20, 100, 200, and 300 K and for $p = 50$ nm measured at 300 K (dotted line). The inset shows the variation of the coercive field with temperature; the experimental results (black curve) are compared with theoretical predictions (red curve). (b) Variation of coercivity as a function of the angle of the applied field measured at 20 K and 300 K for 100 nm lateral size bumps and at 300 K for 50 nm lateral size bumps with a Co/Pt multilayer deposited on top. The black continuous line is the prediction of switching field in the Stoner-Wohlfarth model.

At 300 K, the loop shows a fully saturated magnetization at remanence but the reversal branches are quite sheared. The coercive field is 80 mT. For comparison, the [Co/Pt] film deposited on a flat Si substrate shows a much sharper reversal and a much lower coercive field of only 12 mT (see Fig. 2). Such a difference between the bumpy sample and the flat sample reveals a change of magnetization reversal mechanism, as already reported in Ref. [12]. In the flat film, nucleation of one or some reversed domains occurs at low anisotropy spots and magnetization reversal proceeds through propagation of the domain walls over the whole sample. In the bumpy sample, the reversal takes place dot by dot due to a partial exchange decoupling between the bumps, as explained in Refs. [12] and [15]. This dot-by-dot reversal will be demonstrated in the following by the MFM measurements. The evolution of the coercivity as a function of magnetic field angle with respect to the surface normal is presented in Fig. 3(b). The coercivity decreases when the field angle increases from 0° to 45° and then increases again from 45° up to 75°. Coercivities at 0° and 75° have almost the same value, and the value at 45° is about ¾ of the value at 0°. H_c is considered the switching field of the average dots, and the field angle dependence is to be compared to the two extreme models that characterize a macrospin type

FIG. 2. (Color online) (a) Saturation magnetization vs applied field measured for a [Co(0.4 nm)/Pt(0.7 nm)] $\times$ 4 film at 300 K with out-of-plane (black solid squares) and in-plane (red open circles) field orientation. (b) Saturation magnetization (green solid squares) and anisotropy field (blue open triangles) vs temperature.
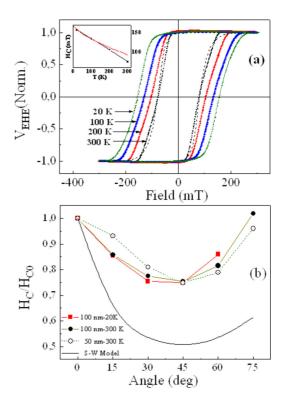
reversal, namely the Stoner-Wohlfarth model [19], and a nucleation/propagation type reversal, namely the Kondorsky model [20]. The experimental curve, close to the Stoner-Wohlfarth model but with a shallower variation, is typical of a dot-by-dot reversal but with a nucleation/propagation process for each dot [21,22]. This argument is corroborated by the low value of H_c (80 mT) as compared to the anisotropy field (470 mT) extracted from the hard axis loop measured on the flat film with SQUID-VSM. In addition to regular anisotropy dispersion, our system shows many reasons for having non-uniform reversal within each dot. First simulations in Ref. [23] show that the curvature of the bump can modify the ideal Stoner-Wohlfarth field angle dependence. Second, the close packing of the bumps induces a strong dipolar interaction between bumps with a gradient of dipolar field inside each bump. Third, the CoPt phase between the bumps must play a strong role through a remaining interdot exchange coupling, similarly to the ion milled edges in Ref. [24] or the irradiated region in Ref. [25].

Changing the temperature from 300 K to 20 K does not drastically affect the hysteresis loop shape or the field angle dependence of the coercivity [Figs. 3(a) and 3(b)]. As the temperature decreases from 300 K, the main change concerns the value of the coercive field, which linearly increases up to 160 mT at 20 K [inset Fig. 3(a)]. This can be understood by the continuous reduction of thermal effects acting on the nucleation process. Since the coercivity's angular dependences at 300 K and 20 K are very similar [Fig. 3(a)], no change in the reversal process is expected in the low temperature range. In the inset of Fig. 3(a), the coercive field changes as a function of temperature and is compared with the theoretical variation predicted by the Sharrock equation [26] in the case of the Stoner-Wohlfarth-like reversal of a nucleation volume V of anisotropy $K(T)$ and magnetization $M_s(T)$ that depend both on temperature T. We used similar parameters as those in Ref. [24]: the applied field time $\tau = 10$ s, the attempt frequency $f_0 = 10$ GHz, and a nucleation volume $V = 15 \times 15 \times 4.4$ nm^3. 15 nm corresponds to an upper value for the exchange length. The experimental anisotropy $K(T)$, extracted from Fig. 2(b), needs to be divided by three since H_c is much lower than H_k^{eff}. Such a factor is typical of real samples where the reversal process starts at a place where the anisotropy is weaker [24,26–29]. Although the fit is clearly not perfect (it cannot be since the reversal is not macrospinlike), the amplitude of the H_c variation with temperature using the Sharrock equation is of the right order of magnitude.

In Figs. 3(a) and 3(b), we also compare the magnetic features of 100 nm and 50 nm period nanobump arrays at 300 K. Their hysteresis loops are similar and coercive fields are identical. The reversal process seems unaffected by the difference in dot diameter at these sizes. The 50 nm period array has just a slightly sharper reversal and slightly larger end reversal tail that may mark a slightly stronger exchange between bumps. Such similar behaviors for the 100 nm and 50 nm period arrays tend to confirm a reversal process beginning at a nucleation region whose diameter is smaller than 50 nm [29]. In the following we will focus only on the 100 nm period media that is much easier to image with high resolution by MFM.

In order to characterize BPM switching and especially SFD of BPM systems, one usually takes the derivative of
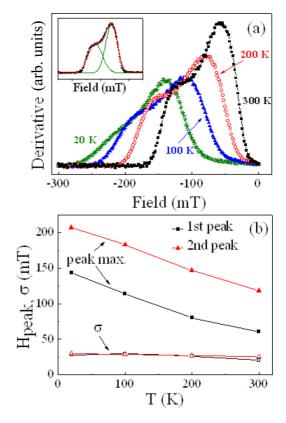

FIG. 4. (Color online) (a) Derivative of EHE loops for Co/Pt multilayers on a 100 nm period bump surface measured at 20, 100, 200, and 300 K. The inset shows the double peak Gaussian fitting of the curve derived from the measurement made at 300 K for $p = 100$ nm. (b) Variation of both peaks' maximum and σ, the standard deviation, as a function of temperature for the first and second peaks shown in (a).

the hysteresis loop reversal branches and uses a Gaussian fit to extract the single peak maximum field and the standard deviation σ of this single peak [18]. Figure 4(a) shows the derivatives for the descending branches of loops shown in Fig. 3(a). For all temperatures, the derivative curve shows a double peak typical of a two step reversal. As will be confirmed later by the MFM images, the double peak feature in the derivative reveals the competition between exchange coupling and strong dipolar interactions. Similar competition affects PMA continuous films, like Co/Pt thin films. Tuning the dipolar field energy to a value of the same order as the exchange coupling energy leads to a double peak derivative whose first peak usually occurs before reaching zero field coming from the saturation field [30,31]. Note that the double peak derivative is observed for continuous films of Co(0.4 nm)/Pt(0.7 nm) multilayer (i.e., the composition we are using here) having around 20 repeats [30], whereas our sample only holds four repeats. Therefore, in our sample the dipolar interactions are more effective, which implies a strong reduction of the interbump exchange coupling in our bump array. Recently, a shallow double peak shape of the hysteresis loop derivative, centered on the coercive field, has also been reported in a BPM with large interbit dipolar interactions and possibly under-etching, i.e., a nonzero interdot exchange coupling [32].
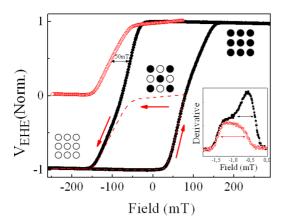
FIG. 5. (Color online) EHE measurement of out-of-plane major (black curve) and one minor loop (red dashed line) for Co/Pt nanobump array. Open red disks show the minor loop (red dashed line) upshifted. The large black and white dots are a scheme of magnetic configuration discussed in the text. Inset: derivative of the open red disks curve (upshifted minor loop) and of black curve (major loop). The arrows point out the difference of "easy switcher" switching field distribution as a function of their magnetic environment.

If the interbump exchange coupling is difficult to extract and quantify here, the strong influence of dipolar interactions acting as a long-range antiferromagnetic coupling is easy to demonstrate. In Fig. 5, the reversal fields of the first 50% of magnetic bits are compared when they have two different environments [18]. From positive saturation, the magnetization reversal of the 50% easiest switchers occurs in negative fields. These switches align the bumps in negative field direction and antiparallel to the remaining bumps. A comparison with the switching of the remaining 50% of the bumps can be made by starting from negative saturation, going to the (positive) fields that reverse half the bumps, and subsequently reverting back to negative saturation (dashed line in Fig. 5). Note that in this reversal process, 50% of the bumps align in negative field direction and parallel to the direction of the remaining bumps. A direct comparison between the two reversal branches shows that the reversal from the half-reversed state requires field amplitudes larger by 50 mT on average. Moreover the derivative in the inset of Fig. 5 shows that this reversal is much shallower than the 50% reversal that starts from the saturated state, revealing the influence of the dipolar field on the SFD and possible differences in the reversal mechanism.

Because of its double peak shape, we chose not to fit the hysteresis loop derivative with one Gaussian but with two Gaussian curves [see inset Fig. 4(a)]. We call H_{peak} the fields at the first (lower reversal field) and second peak (larger reversal field) maximum, and we call σ the standard deviation of the first and second Gaussian curve. These parameters are displayed in Fig. 4(b) as a function of temperature. The difference between the two peak H_{peak} values remains constant with temperature, around 60 mT. The σ is very similar for the two peaks. We chose to define SFD as the standard deviation sigma of a function equal to the sum of two Gaussians. At 300 K, SFD is about 37 mT and increases up to 42 mT at 20 K. The increase of SFD with temperature can originate both from the intrinsic SFD (dot-to-dot variation of anisotropy

or magnetization, presence, or absence of misaligned grains) or from the increase of dipolar field induced SFD as M_s increases when the temperature decreases. The SFD value is high as compared with the coercivity value. The relative SFD, i.e., SFD/H_c, is about 46% at 300 K, which is much larger than usual values of approximately 10% found in Co/Pt-based BPM [33,34]. One can wonder if this high relative SFD is mainly the result of a combination of low H_c (related to the low H_k and maybe a specific nucleation process at the bump side), high dipolar fields (related to large Ms), and the close packing of the BPM array, or if the SFD originates from a large dot-to-dot distribution of magnetic features.

In order to further distinguish and quantify the SFD origins, we use the $\Delta H(M, \Delta M)$ method, which allows for separating the intrinsic SFD from interaction effects. Originally, the method had been developed based on the mean-field model of perpendicular magnetic recording media [16,17] and BPM [16,18,35] and was later generalized beyond the mean-field approximation to be reliable in a broader range of exchange and dipolar coupling values [36–38].

The method requires as an input the measurement of a hysteresis loop and a set of recoil curves, such as that shown in Fig. 6(a) for the 100 nm period nanobump array at room temperature. Here, the recoil curves have been generated at reversal fields corresponding to fractions of switched bumps $\eta = 23\%$, 50%, and 70%. The initial step before the actual analysis requires transforming the data set to the $\Delta H(M,$
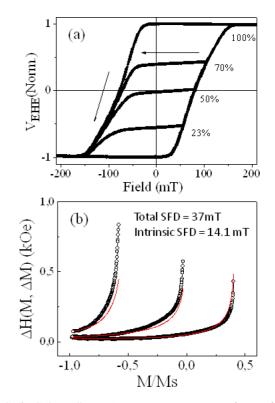

FIG. 6. (Color online) (a) EHE measurement of out-of-plane major and minor loops for Co/Pt nanobump array with $p = 100$ nm. The percentage values correspond to the ratio of switched nanobumps during each loop. (b) $\Delta H(M, \Delta M)$ data (open circles) obtained from the partial reversal curves in (a) and compared with the fit (red solid line) of the $\Delta H(M, \Delta M)$ model. The quality of the fit is attested by the correlation coefficient $R^2 = 0.9689$.
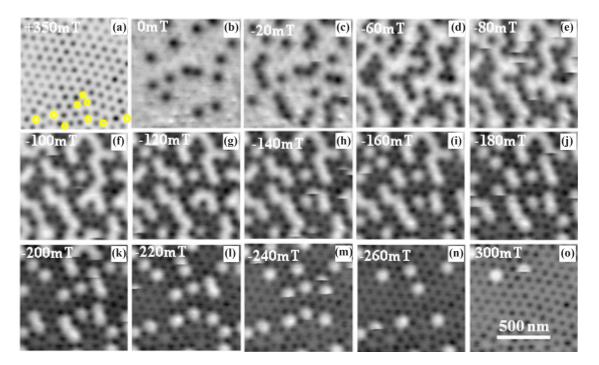
FIG. 7. (Color online) 1 μm $\times$ 1 μm MFM images obtained successively after saturation at +350 mT (a), under 0 mT to −300 mT (b)–(o). Since the magnetization is saturated at −350 mT, (a) corresponds to an average topography signal that is used to correct all the other MFM images. Yellow hexagons in (a) mark lattice stacking faults.

$\triangle M$) form by first inverting the plots, i.e., plotting field H vs M/Ms and then subtracting the field values along a recoil curve from the field values along the adjacent (decreasing) hysteresis loop branch (note the equivalence $M \approx V_{EHE}$ due to the normalization, from which follows $\triangle M = 1 - \eta/100\%$). The results of the transformation are the $\triangle H(M, \triangle M)$ data shown in Fig. 6(b) as open circles. Next, the data are fitted by the set of reference functions of the generalized $\triangle H(M, \triangle M)$ method for variable exchange and dipolar interactions assuming a lognormal intrinsic SFD. The best-fit reference function gives the statistically most reliable estimate of the intrinsic SFD. As shown in Fig. 6(b), the fit is of very good quality with $R^2 = 0.9689$, yielding the standard deviation of the intrinsic SFD equal to $\sigma_{intrinsic} = 14.1$mT. So the $\triangle H(M, \triangle M)$ method demonstrates that the intrinsic SFD is only about one-third of the overall SFD (37 mT) extracted from EHE loop derivative (Fig. 4). The large dipolar effect deduced from the comparison between the macroscopic SFD and the $\triangle H$ method sigma is fully consistent with the large shift highlighted in Fig. 5.

B. Bump-by-bump reversal mechanism imaged by MFM

An improved understanding of the roles of the intrinsic SFD and the dipolar interactions for the magnetization reversal mechanism of Co/Pt nanobump arrays is obtained from a field-dependent MFM study. Figure 7 shows the results obtained for increasing negative fields after saturation in positive fields, and Fig. 7(a) shows the positive saturation image (+350 mT). Black dots visible on a gray background reflect the center positions of the bumps due to van der Waals forces arising from the smaller tip-sample distance. This nonmagnetic contribution has been reduced in the other

MFM figures using the procedure described in Sec. II B. The yellow spots in Fig. 7(a) indicate AAO lattice defect positions. Figures 7(b)–7(o) show MFM images of the same nanobump array region taken under applied fields (i.e., not at remanence) from +350 mT to −350 mT. Figure 7(b) shows data obtained at 0 mT. Fifteen from a total of 131 bumps visible in the image have switched because of their low intrinsic reversal field combined with the dipolar field from the neighboring bumps. Some images show also that the stray field coming from the MFM tip influences the bumps magnetization reversal. The measurements were carried out with a commercial tip, maintaining a tip-sample distance of approximately 8 $\pm$ 1 nm on average. At this distance, the maximum stray fields observed for this class of CoCrPt tips is typically of the order of 5 mT, which adds to the external applied field. As the field amplitude increases from 0 mT towards negative values, more and more black spots occur until all dots have been reversed [see Figs. 7(c)–7(o)]. From the MFM images, we can calculate the normalized magnetization as the number of white bumps minus the number of black bumps divided by the total number of bumps. The calculated values are plotted as a function of applied magnetic field in Fig. 8.

The calculated MFM reversal branch is slightly different from the EHE one. Especially, the two reversal steps are much more visible in the MFM data, and the separation between the two peaks of the reversal branch derivative is much more pronounced than in the EHE data. Half reversal is reached at about 80 mT, which is close to the coercive field value measured by EHE. Nevertheless, the reversal starts slightly before zero field (−20 mT for the EHE measurement) and ends at around −300 mT (−170 mT for the EHE measurement). All these differences must originate from a slightly larger thickness of Co in the sample measured by MFM. Indeed at
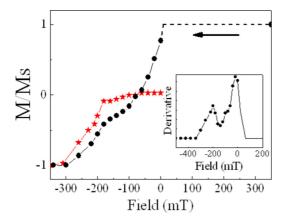
FIG. 8. (Color online) Normalized moment calculated from the MFM images in Fig. 7 as a function of the applied field. Each solid circle corresponds to one MFM image. The dashed line corresponds to a field range where no MFM images have been performed. The arrow shows the field sweep direction. The red stars correspond to the normalized magnetization extracted from MFM images measured during fields applied after out-of-plane demagnetization of the sample. The inset presents the derivative of the solid circle branch.

300 K we measured $M_s = 840$ kA/m (instead of 760 kA/m), and the effective anisotropy field extracted from the in-plane field loop is $H_k^{eff} = 380$ mT (instead of $H_k^{eff} = 470$ mT). As a consequence dipolar field interactions are stronger in the MFM sample, so a stronger shearing of the hysteresis loop branches is measured. The discrepancy may also be an artifact caused by the fact that MFM images comprise only about 131 bumps, whereas EHE senses millions of bumps.

Let us now analyze in more detail the MFM images to get a deeper understanding of the reversal mechanism. First, from all images, we can deduce that there are only two possible magnetic states for each bump, i.e., fully magnetized up or fully magnetized down. A nonuniform magnetization state is not observed. We can also conclude that the magnetization reverses bump by bump. Nevertheless, both exchange coupling and dipolar fields affect the location of a bump reversal. From 0 mT [Fig. 7(b)] to −20 mT [Fig. 7(c)], 15 additional bumps have switched over 116 unswitched (white) bumps. If we do not consider the bumps at the image edges (because we do not know the magnetic states of all their neighbours), we have to consider only 85 unswitched bumps at 0 mT. Of these 85 unswitched bumps, 58 have at least one switched neighbor, and 27 have none. Nevertheless, of the 12 reversals (3 reversals occur at the image edge that we disregard), 8 occur next to a switched neighbor, and 4 happen in unswitched regions. The switching event location seems to be uncorrelated to the presence or the absence of switched neighbors. This result indicates that although the long-range dipolar fields affect the bump reversal (Fig. 5), locally the interbump exchange coupling and the dipolar interaction more or less compensate each other. Furthermore, we can also conclude that the dipolar field opposes the exchange coupling since the subsequent switching events do not lead to an isotropic growth of a reversed domain but tend to form lines of switched bumps having a width of one bump [Figs. 7(c) and 7(d)]. At −80 mT [Fig. 7(e)], where half of the bumps have switched,

a labyrinthine pattern is observed, similar to what can be observed in Co/Pt continuous films. In that these patterns arise from a competition between short-range order (exchange coupling) and long-range order (dipolar coupling), they are reminiscent of patterns formed in a large range of physical systems, e.g., Langmuir films, diblock copolymers, chemical mixtures, and magnetic thin films [39,40–42]. As in PMA continuous thin films, the method of sweeping the field from the saturated magnetic configuration, the presence of thermal fluctuations and the intrinsic SFD prevent the system from reaching the well-ordered stripes' domain state [43–45]. Section III C is devoted to a deeper investigation of the stability of zero-magnetization configurations.

After the system has reached the labyrinthine state at −80 mT [Fig. 7(e)], the magnetic susceptibility strongly decreases, and only 14 bumps switch between −100 mT and −180 mT (for comparison, 15 bumps switch between 0 and −20 mT or between −20 and −40 mT). At this stage the reversal process consists in magnetization reversal mostly for the bumps having two or three unswitched neighbors (11 bumps over 14 to reverse). Here dipolar fields undoubtedly counteract the interbump exchange coupling; otherwise, the latter would have prevented the system from creating more switched/unswitched transitions, and white lines would have shrunk from their ends. We believe that the increase of switched/unswitched walls is the main origin of the slowdown in switching. After the field has been ramped to −200 mT, the magnetic susceptibility increases again. Almost all unswitched bumps are now surrounded by switched bumps, and all have comparable dipolar and exchange coupling energy. So, the intrinsic SFD becomes the leading parameter selecting the switching order.

We earlier used the $\Delta H(M, \Delta M)$ method to show that about one-third of the total SFD (14.1 mT) is intrinsic. With the MFM images in Fig. 7, we can now try to get more insight on the impact of the intrinsic SFD on the magnetic configurations during field cycling. Easy and hard switchers (i.e., bumps having the lowest and largest switching field, respectively) can be detected by the observation of successive images during field sweeps. Three magnetic field cycles have been used to define the easy switchers as the bumps that have at least a 66% chance to be already switched at zero field starting from a saturated state (8 over about 150 bumps in the whole image). We defined the hard switchers as the bumps that have at least a 66% chance of remaining unswitched at −260 mT (9 over about 150 bumps in the whole image). Easy and hard switchers' positions are highlighted in the MFM image in Fig. 9(a), which has been taken around half reversal (60 mT) after negative field saturation. At this stage of the reversal process, they belong to a labyrinthine domain pattern composed largely of black and white straight lines. In this pattern, all the easy switchers are black, and all hard switchers are white. On the same image [Fig. 9(a)], we have also placed the position of the self-organized AAO network stacking faults [as well as in Fig. 7(a)]. Easy and hard switchers' locations are clearly uncorrelated with the stacking defects. The dispersion in bump diameter is in our back AAO template of the order of ±9 nm (cf. AFM processing in Sec. III D). We were not able to correlate easy or hard switchers to a larger or smaller bump diameter nor to specific bump shape. Since the reversal
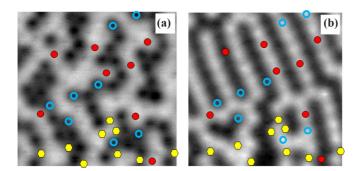
FIG. 9. (Color online) $1\,\mu\text{m} \times 1\,\mu\text{m}$ MFM images obtained close to half reversal (-60 mT) after negative field saturation (a) and at remanence after demagnetization (b). The solid red disks correspond to hard switchers, open blue disks to easy switchers, and yellow hexagons to topological defects.

of a bump does not occur by coherent reversal, we do not expect the bump diameter to affect the field of nucleation. As a consequence, we expect the intrinsic SFD to originate mostly from the presence, absence, number, and location of Co/Pt [100] misoriented grains on the bumps that differ from one bump to another [27–29]. The location of easy and hard switchers clearly constrains the shape and location of the black and white domains in the labyrinth pattern of Fig. 9(a). During a field cycle, the magnetic configurations at 50% reversal in the ascending and descending branches are not identical. Less than 10% of bumps change from one MFM image to another one. So, the switching process is not fully deterministic, and thermal fluctuations slightly affect the 50% reversal magnetic configurations.

C. Influence of dipolar frustrations, exchange-coupling, and intrinsic SFD on zero-magnetization states

In Fig. 9, we compare the MFM images measured under a perpendicular field of -60 mT after positive saturation at $+350$ mT [Fig. 9(a)] and one measured at remanence after ac demagnetization under decreasing out-of-plane field [Fig. 9(b)]. Unlike the labyrinth pattern discussed above, out-of-plane ac demagnetization leads to a mostly well-ordered succession of up and down magnetized stripes. Each stripe consists of a 1D chain of bumps. The width of both serpentine domains and stripe domains, mostly of the order of the array period, corroborates our previous comparison between the nanobump assembly and the [Co(0.4)/Pt(0.7)]$_{20}$ multilayer thin film (see Sec. III A) and the strong decrease of lateral ferromagnetic exchange-coupling in our AAO system. Indeed 100 nm domain periods would require 20 to 40 repeats in a strongly coupled thin film [30]. Nevertheless, it is interesting to note that a well-ordered stripe configuration in strongly coupled PMA thin films is only observed after in-plane field ac demagnetization [30,46]. Here all demagnetization processes, with a careful orientation of the external field to as close as possible to the normal to the film have led to a stripe state. This result proves that our bump assembly is not directly comparable to regular Co/Pt thin films. Another parameter has to be considered in the energy calculation to explain the stripe state stability of Fig. 9(b).

The main difference between the nanobump array and the usual continuous film lies in the triangular lattice of the AAO template. The loss of isotropy has an important impact since the triangular lattice generates a dipolar field frustration between neighboring bumps' magnetization. Frustration of magnetic spins interacting through dipolar fields in triangular spin lattice has been heavily studied since the 1950s [47,48] and remains a subject of current investigation due to the development of micro- and nanopatterning techniques [1,49,50]. Kireev *et al.* [51] have recently reported a work that is particularly well suited to help understanding the consequences of dipolar frustrations in our bump assembly. They demonstrate that the ground state of an assembly of hexagonal array of perpendicularly magnetized Ising spins interacting only through the antiferromagnetic dipolar interactions consists in a series of uniformly magnetized stripes of spins, each stripe being oppositely magnetized to its neighboring stripes. This conclusion holds for pure dipolar interactions. If a ferromagnetic coupling between closest neighbors has to be considered, the fundamental state is modified and should evolve towards wider domains. To quantify this effect, the lowest energy configuration has been determined for a small network of 25 elements for various coupling coefficients between first neighbors. With the unit of coupling coefficients chosen to be the dipolar coupling between first neighbors, $J_1 = -1$ corresponds to the pure dipolar coupling between bumps and leads to single bump wide stripes, as shown in the scheme in Fig. 10(a). This structure is unchanged until the first-neighbors coupling reaches -0.2, where magnetic bands are no longer one dot wide [Fig. 10(b)]. Indeed at that point, in a real system, the ferromagnetic coupling between first neighbors would almost compensate the first-neighbors dipolar interaction. As the relative ferromagnetic coupling increases, passing through exact compensation at $J_1 = 0$ and until $J_1 = +0.5$, the domains get wider and wider [see Figs. 10(d) and 10(e)]. At $J_1 = +1$, the fundamental state is a fully saturated state. We can conclude from our calculation that the presence of a "small" direct ferromagnetic exchange coupling between dots does not affect the nature of the fundamental state, so that single bump wide stripes are stabilized by the triangular lattice of the bump assembly, which does not exist in a regular full film deposited on flat substrate.
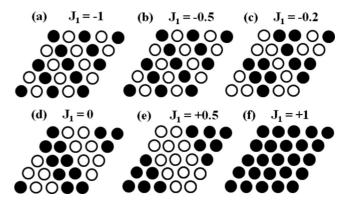

FIG. 10. Ground states for characteristic values of first-neighbors magnetic coupling J_1 with the unit of coupling coefficient being the dipolar coupling between first neighbors; e.g., (a) holds only dipolar couplings.
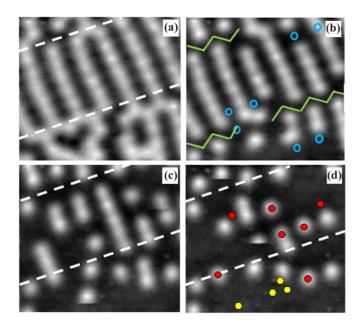
FIG. 11. (Color online) 1 μm × 1 μm MFM images obtained at remanence after out-of-plane demagnetization (a) and then under −180 mT (b), −210 mT (c), and −250 mT (d), respectively. The red solid disks correspond to hard switchers, blue open disks to easy switchers; the green lines highlight specific switched regions, and the yellow hexagons correspond to stacking defects, as discussed in the text. The white dashed lines mark the region taken into account to calculate the relative magnetization in Fig. 8.

The well-ordered stripe configuration does not cover the whole MFM image of Fig. 9(b). Stripes have finite length, as later highlighted by the two dashed lines in Fig. 11(a). Higher energy configurations are observed. In the disordered region, as in the ordered one, intrinsic SFD does not seem to constrain the final stripe domains state since up and down magnetized easy and hard switchers can be found in Fig. 9(b). On the contrary, it seems reasonable to think that part of the magnetic disorder originates from the large density of bump packing faults (i.e., change of dipolar environment) present in the lower part of the MFM image. The short- and long-range influence of these structural defects will be described in Sec. III D. In addition, white zigzag stripes spread perpendicularly to the stripes. This topological magnetic defect typically originates from a succession of Y-shaped domains that connect stripes laterally shifted from one bump. This can be clearly observed around the bottom white dashed line in Fig. 9(b). Such a zigzag domain can be modeled by accounting for dipolarly coupled Ising spins [51], but it is of course stabilized if direct ferromagnetic exchange-coupling exists between neighboring bumps.

Let us now try to quantify the field stability of the stripe domains' configuration as compared to the labyrinth one. In Fig. 11, we show MFM images measured when an external magnetic field is applied onto the ac demagnetized remanent state. Figure 11(a) corresponds to the same image of the ac demagnetized state as Fig. 9(b). The two dashed lines in Figs. 11(a), 11(c), and 11(d) delimitate the zone of the well-ordered stripes state (70 bumps total) that has been taken into account for calculating the magnetization vs the field

reported in Fig. 8. As the field increases, the stripe state region is almost unchanged up to −180 mT. Only 4 of 35 unswitched (white) bumps have switched. Only one of these 4 bumps has previously been identified as easy switcher. At this stage, under −180 mT, this region holds 31 unswitched bumps. For a fair comparison, the same region in Fig. 7(j) holds only 21 unswitched bumps. This difference is highlighted in the calculated magnetization vs field curves in Fig. 8, where the two curves are quite different. We can conclude that a larger field amplitude is required to destroy the zero-magnetization stripe state than the zero-magnetization labyrinth state. It is consistent with the fact that the stripe state is the energy ground state. As expected on the same field range from 0 to −180 mT, some bumps have switched outside the stripe region. They are either easy switchers or, more interestingly, bumps connecting the shifted stripes. In Fig. 11(b), the new boundary between the shifted stripes is marked with a green zigzag. Again, as described in Ref. [51], this zigzag composed of switched bumps is stabilized by the external field, which is competing with the dipolar antiferromagnetic interactions. Further increase of the field leads to successive switching events of individual bumps inside the unswitched stripes until only mostly hard switchers remain. This stage of the process is essentially similar to the one reported in Figs. 7(j)–7(o).

D. Influence of arrays ordering faults on the zero-magnetization configurations

We have demonstrated above that the intrinsic SFD is uncorrelated with the stacking defects of the nanobump array. However, in the self-assembly of BPM, bit location and ordering faults are known to be important for achieving tight magnetic SFD and reliable control of the magnetic configuration [8,52]. Moreover, the number of spins, the finite size, and possible distortion of the well-ordered triangular array of Ising spins is found to affect the energy (and thus the stability) of the various frustrated magnetic states [51,53]. In Fig. 9(b), we have already noticed that the lower zone of the MFM image, which contains a large number of stacking defects (yellow spots), has a much less ordered magnetic configuration, i.e., no well-ordered stripe domains, as compared to the upper part of the image where there is no lattice defect.

To gain more insight into the role of stacking defects in the array on the magnetic ground state, we demagnetized the first sample (used for EHE measurement) with perpendicular fields and imaged with AFM and MFM a region of the sample with a large density of ordering defects. MFM and AFM at the same sample place (2 μm × 2 μm) are shown in Figs. 12(a) and 12(b), respectively. The resulting MFM pattern [Fig. 12(a)] is superimposed on the AFM image in Fig. 12(b) for further processing of the images. Let us use the AFM image to locate the magnetic bump centers and to characterize the lattice ordering (Fig. 13). First a Delaunay triangulation is applied to the set of bump centers so that the whole surface is covered by triangles. After the triangulation, one can define the structural bump-ordering quality, which is related to the triangle quality by imposing criteria on the triangle edges in such a way as to keep only triangles that are equilateral within a defined tolerance. The criteria are defined as follows [see Fig. 13(b) for
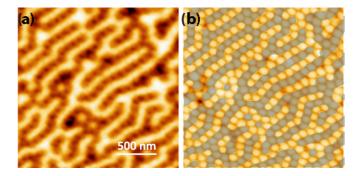
FIG. 12. (Color online) (a) MFM image of a 2 μm $\times$ 2 μm array of bumps sample surface. (b) Corresponding 2 μm $\times$ 2 μm AFM image with the MFM pattern superimposed on it.

notation]:

$$Cr_1 = \max(abs([d_1, d_2, d_3]))/\text{mean}([a,b,c])$$

where

$$d_1 = a - b, \quad d_2 = a - c, \quad d_3 = b - c,$$

$$Cr_2 = 1 - \min([a,b,c])/\max([a,b,c]),$$

$$Cr_3 = \max(abs(\pi/3[\alpha,\beta,\gamma]))/(\pi/3).$$

An additional criterion over the surface is used to avoid the appearance of aberrant triangles, meaning triangles satisfying the three criteria above but having a surface much larger than the mean triangle surface. Triangles are accepted when their surface differs from the mean surface by less than two times the standard deviation, i.e., $S \in [S - 2\sigma S, S + 2\sigma S]$. Introducing the tolerance τ the final selection conditions become

$$(Cr_1 < \tau) \cap (Cr_2 < \tau) \cap (Cr_3 < \tau) \cap (S \in [S - 2\sigma_S, S + 2\sigma_S]).$$

Applying a tolerance of 30% ($\tau = 0.3$) in the above equation, one obtains 71.6% (587/820) of triangles satisfying the criteria [see Fig. 13(a)]. Computing the statistics over the
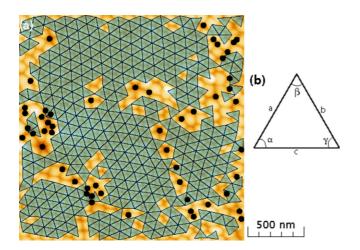

FIG. 13. (Color online) (a) AFM image with additional black filled circles showing structural defaults. The triangles obtained by Delaunay triangulation applied to the bump center coordinates are filtered using criteria from Eq. (1) at $\tau = 0, 3$ level and superimposed on the AFM image. (b) Sketch of an equilateral triangle showing the angles and edges notations.
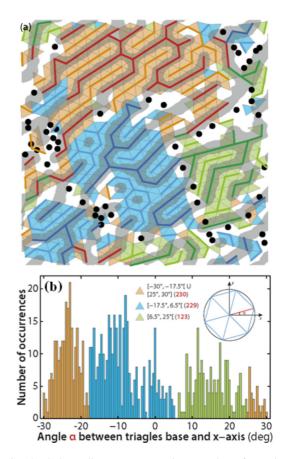

FIG. 14. (Color online) Postprocessing results after triangles base angle (α) analysis giving rise to three main base angle orientations according to the number of occurrences distribution of the α angle. The three different base angle orientations correspond to different magnetic domains delimited by the structural defects (black filled circles). Domains with orange triangles correspond to α ranging from $-30°$ to $-17.5°$, from 25° to 30°, the ones with blue triangles correspond to α ranging from $-17.5°$ to 6.5°, and the ones with green triangles correspond to α ranging from 6.5° to 25°. (b) Number of occurrences of a given base angle α ranging from $-30°$ to 30° ($\Delta\alpha = 60°$). In the inset, triangle base angle α definition showing the six equivalent triangles (due to hexagonal symmetry) for a given α base orientation relative to the x axis. The angle range for the triangle base is then limited to 60° (360°/6) due to symmetry.

triangles' edges one obtains a mean interbump distance of 103.8 nm with a standard deviation of 9.0 nm. As shown in Fig. 13(a) by black filled circles, the structural defaults are almost outside the surface covered by the equilateral triangles satisfying the criteria detailed above (at level $\tau = 0.3$). The quality of the equilateral triangles informs on the structural ordering of the array of bumps and allows pointing out the lattice defects. Although some hole locations seem stochastic over the whole sample, Fig. 13(a) clearly demonstrates that lines of holes form boundaries between well-ordered areas.

To go further in characterizing the features of the different ordered areas, a triangle base angle analysis is performed. Due to hexagonal symmetry in the bumps' ordering, there are six nominally equivalent triangles corresponding to a given α base angle relative to the x axis, as shown in Fig. 13(b). Figure 14(b)

shows the number of occurrences of a given α base angle in the range $-30°$ to $30°$ ($\Delta\alpha = 60°$). From the latter result three main base angle orientations are distinguished using three colors: orange for $\alpha \in [-30°' -17.5°] \cup [25°, 30°]$, blue for $\alpha \in [-17.5°' 6.5°]$, and green for $\alpha \in [6.5°' 25°]$. Then, using the same color code to fill in the corresponding triangles, one obtains a few colored regions on the AFM image [Fig. 14(a)]. At this point we can distinguish different "hyper grains" (ordered regions of different colors) defined by their respective orientation (α). The morphology of our surface thus mimics the surface of (111) textured body-centered-cubic (bcc) polycrystals. The MFM demagnetized state pattern is then superimposed on the colorized AFM image on Fig. 14(a).

From the MFM-AFM image comparison, it is clear that the magnetic lines are oriented along the α angle (modulo $2\pi/3$) characterizing the hyper grain which they belong to. Hyper grain boundaries formed by a line of unique defects seem not to affect the magnetic stripe too much. When passing through a single defect boundary, the magnetic stripe just deviates to a new direction. The interbump exchange coupling may help to stabilize the boundary crossing. Zones with packed defects affect the magnetic configuration more due to a strong change in the exchange coupling and dipolar field environment, as observed in both Figs. 9(b) and 14(a). The remaining question is whether the magnetic Y-shaped domains and zigzag domain shape located inside the hyper grains are due to the finite size of the hyper domain [51], due to lattice stress [53], or due to another feature. More statistics on hyper domain size and shape are required to conclude on this point.

IV. SUMMARY AND CONCLUSIONS

In our recent paper [12], we presented a method to grow a perpendicularly magnetized BPM system, i.e., an ordered assembly of magnetic islands. It was achieved by depositing a Co/Pt multilayer on top of the barrier layer of AAO templates with a 100 nm period to form an ordered array of ferromagnetic nanodots, so-called nanobumps. Our self-assembly method would have a number of advantages over the lithographic-based methods, including low cost and extremely simple processing. The AAO nanotemplates would display tunable geometrical parameters, mild preparation conditions, robustness, and resistance to high temperatures. In addition, the extremely small attainable interbump period constitutes substantial advantages. Indeed regular nanopore arrays in AAO with ultrasmall pore diameter (even less than 10 nm) and pore interdistance as small as 15 nm have already been demonstrated [54,55].

In the present paper, we have studied in detail two magnetic features of a [Co(0.4 nm)/Pt(0.7 nm)]$_4$ multilayer deposited on top of 100 nm and 50 nm AAO nanotemplates. EHE and SQUID-VSM reveal values of coercivity five times lower than the anisotropy field. The latter's dependence on field angle and as a function of temperature reveal an incoherent magnetization-reversal mechanism, most probably based on a nucleation-propagation process inside each bump, as usually observed in nano-objects of this size. Surprisingly, the derivative of the hysteresis loops shows a double peak structure that cannot be explained by taking into account only interbump dipolar

fields. One has to consider an additional interbump exchange coupling [31]. Nevertheless, such a double peak structure requires 20 repeats of the same Co(0.4 nm)/Pt(0.7 nm) bilayer as a thin film [30], whereas our bump array is only covered with four repeats of Co(0.4 nm)/Pt(0.7 nm). Therefore, we can conclude that the exchange coupling is strongly reduced in our bumpy system as compared to a continuous film. Intermixing between the bumps is the most probable origin of this partial exchange decoupling, as explained in Ref. [15]. High-resolution MFM allowed imaging the magnetization reversal over hundreds of bumps during sweeps of an external magnetic field of uniform value over the whole imaged area. Bump-by-bump individual magnetization switching is demonstrated. After the first switching events, competition between exchange coupling and dipolar interaction is found to favor lines of switched bumps until 50% of the bumps have been switched. At this stage, a labyrinthine domain pattern is observed that has a low field susceptibility, i.e., it is more stable than the previous and subsequent configuration. This loss of magnetic susceptibility at 50% reversal leads to the double peak feature of the macroscopic hysteresis loops. Using an out-of-plane demagnetization, we achieved a zero-magnetization configuration consisting of successive black and white stripes with only one bump width. This configuration is even more stable than the labyrinthine one. When considering each bump magnetization as an Ising spin, the dipolar interactions in a triangular lattice are sufficient to explain the stability of the stripe state. Nevertheless, this configuration stability is not drastically affected by the nonvanishing interbump exchange coupling as long as it remains less than a fourth of the dipolar interactions amplitude.

Magnetometry and MFM measurements have been used to quantify the SFD, to locate easy and hard switchers, and to distinguish the different origins of SFD and their influence on the magnetic configurations. The $\Delta H(M, \Delta M)$ method shows that the intrinsic SFD is only one-third of the total SFD. We could not find any structural reason to explain easy and hard switchers' locations, so we conclude that the intrinsic SFD mostly comes from misoriented Co/Pt grains inside the bumps [27,28]. The strong dipolar-induced SFD is due to the close packing of the AAO template and might be a showstopper for a BPM technology implementation. In addition, AAO lattice stacking faults are found to form mostly boundaries between well-ordered bump arrays. Lines of single defects seem not to drastically affect the magnetic features of the neighboring bumps, whereas larger defect density does.

Finally, magnetic features of our nanobump assembly are very similar to those observed in continuous PMA thin films. Therefore, besides being interesting as support for a BPM template, we think that the present AAO system could be a model for getting a deeper understanding of the influence of the different thin film parameters (exchange coupling, dipolar interaction, and, more importantly, intrinsic SFD or thermal fluctuations) on the reversal mechanisms in PMA films [30,38,43,44]. Two main advantages of the bump assembly system would be the control of interbump exchange coupling and the precise characterization of SFD, which is difficult in usually strongly coupled systems [43,56]. More generally, the present nanobump array is also a rich parameter space for

testing in more detail isotropic and anisotropic triangular Ising models with short- and long-range interactions [49,57] that rule a wide range of physical systems such as Langmuir films, diblock copolymers, chemical mixtures, and not only magnetic thin films [39–41].

ACKNOWLEDGMENTS

[1] R. F. Wang, C. Nisoli, R. S. Freitas, J. Li, W. McConville, B. J. Cooley, M. S. Lund, N. Samarth, C. Leighton, V. H. Crespi, and P. Schiffer, Nature (London) **439**, 303 (2006).

[2] S. Zhang, J. Li, I. Gilbert, J. Bartell, M. J. Erickson, Y. Pan, P. E. Lammert, C. Nisoli, K. K. Kohli, R. Misra, V. H. Crespi, N. Samarth, C. Leighton, and P. Schiffer, Phys. Rev. Lett. **109**, 087201 (2012).

[3] T. R. Albrecht, D. Bedau, E. Dobisz, Gao He, M. Grobis, O. Hellwig, D. Kercher, J. Lille, E. Marinero, K. Patel, R. Ruiz, M. E. Schabes, Wan Lei, D. Weller, and Wu Tsai-Wei, IEEE Trans. Magn. **49**, 773 (2013).

[4] O. Ozatay, P. G. Mather, J. U. Thiele, T. Hauet, and P. M. Braganca, Spin-Based Data Storage, in *Nanofabrication and Devices*, Vol. 4, of Comprehensive Nanoscience and Nanotechnology, D. Andrews, G. Scholes, and G. Wiederrecht, eds. (Elsevier, London, 561, 2010).

[5] S. Y. Chou, Proc. IEEE **85**, 652 (1997).

[6] F. Luo, L. J. Heyderman, H. H. Solak, T. Thomson, and M. E. Best, Appl. Phys. Lett. **92**, 102505 (2008).

[7] C. A. Ross, H. I. Smith, T. A. Savas, M. Schattenberg, M. Farhoud, M. Hwang, M. Walsh, M. C. Abraham, and R. J. Ram, J. Vac. Sci. Technol. B **17**, 3168 (1999).

[8] O. Hellwig, J. K. Bosworth, E. Dobisz, D. Kercher, T. Hauet, G. Zeltzer, J. D. Risner-Jamtgaard, D. Yaney, and R. Ruiz, Appl. Phys. Lett. **96**, 052511 (2010).

[9] M. Albrecht, G. Hu, I. L. Guhr, T. C. Ulbrich, J. Boneberg, P. Leiderer, and G. Schatz, Nature Mater. **4**, 203 (2005).

[10] L. Yan, K. Wang, J. Wu, and L. Ye, Colloids and Surfaces A: Physicochem. Eng. Aspects **296**, 123 (2007).

[11] P. Kappenberger, F. Luo, L. J. Heyderman, H. H. Solak, C. Padeste, C. Brombacher, D. Makarov, T. V. Ashworth, L. Philippe, H. J. Hug, and M. Albrecht, Appl. Phys. Lett. **95**, 023116 (2009).

[12] L. Piraux, V. A. Antohe, F. Abreu Araujo, S. K. Srivastava, M. Hehn, D. Lacour, S. Mangin, and T. Hauet, Appl. Phys. Lett. **101**, 013110 (2012).

[13] H. Masuda and K. Fukuda, Science **268**, 1466 (1995).

[14] O. Rabin, P. R. Hertz, Y.-M. Lin, A. I. Akinwande, S. B. Cronin, and M. S. Dresselhaus, Adv. Funct. Mater. **13**, 631 (2003).

[15] T. C. Ulbrich, C. Bran, D. Makarov, O. Hellwig, J. D. Risner-Jamtgaard, D. Yaney, H. Rohrmann, V. Neu, and M. Albrecht, Phys. Rev. B **81**, 054421 (2010).

[16] A. Berger, Y. H. Xu, B. Lengsfield, Y. Ikeda, and E. E. Fullerton, IEEE Trans. Magn. **41**, 3178 (2005).

[17] A. Berger, B. Lengsfield, and Y. Ikeda, J. Appl. Phys. **99**, 08E705 (2006).

[18] O. Hellwig, A. Berger, T. Thomson, E. Dobisz, Z. Z. Bandic, H. Yang, D. S. Kercher, and E. E. Fullerton, Appl. Phys. Lett. **90**, 162516 (2007).

[19] E. C. Stoner and E. P. Wohlfarth, Philos. Trans. R. Soc. London A **240**, 599 (1948).

[20] E. Kondorsky, J. Phys. Moscow **2**, 161 (1940).

[21] R. Dittrich, G. Hu, T. Schrefl, T. Thomson, D. Suess, B. D. Terris, and J. Fidler, J. Appl. Phys. **97**, 10J705 (2005).

[22] J. W. Lau, X. Liu, R. C. Boling, and J. M. Shaw, Phys. Rev. B **84**, 214427 (2011), and references therein.

[23] T. C. Ulbrich, D. Makarov, G. Hu, I. L. Guhr, D. Suess, T. Schrefl, and M. Albrecht, Phys. Rev. Lett. **96**, 077202 (2006).

[24] J. M. Shaw, S. E. Russek, T. Thomson, M. J. Donahue, B. D. Terris, O. Hellwig, E. Dobisz, and M. L. Schneider, Phys. Rev. B **78**, 024414 (2008).

[25] T. Aign, P. Meyer, S. Lemerle, J. P. Jamet, J. Ferré, V. Mathet, C. Chappert, J. Gierak, C. Vieu, F. Rousseaux, H. Launois, and H. Bernas, Phys. Rev. Lett. **81**, 5656 (1998).

[26] M. P. Sharrock and J. T. McKinney, IEEE Trans. Magn **17**, 3020 (1981).

[27] J. W. Lau, R. D. McMichael, S. H. Chung, J. O. Rantschler, V. Parekh, and D. Litvinov, Appl. Phys. Lett. **92**, 012506 (2008).

[28] B. Pfau, C. M. Gunther, E. Guehrs, T. Hauet, H. Yang, L. Vinh, X. Xu,, D. Yaney, R. Rick, S. Eisebitt, and O. Hellwig, Appl. Phys. Lett. **99**, 062502 (2011).

[29] J. M. Shaw, M. Olsen, J. W. Lau, M. L. Schneider, T. J. Silva, O. Hellwig, E. Dobisz, and B. D. Terris, Phys. Rev. B **82**, 144437 (2010).

[30] O. Hellwig, A. Berger, J. B. Kortright, and E. E. Fullerton, J. Magn. Magn. Mater. **319**, 13 (2007), and references therein.

[31] A. Berger and H. Hopster, J. Appl. Phys. **79**, 5619 (1996).

[32] N. Eibagi, J. J. Kan, F. E. Spada, and E. E. Fullerton, IEEE Magnetic Lett. **3**, 4500204 (2012).

[33] O. Hellwig, T. Hauet, T. Thomson, E. Dobisz, J. D. Risner-Jamtgaard, D. Yaney, B. D. Terris, and E. E. Fullerton, Appl. Phys. Lett. **95**, 232505 (2009).

[34] T. Hauet, E. Dobisz, S. Florez, J. Park, B. Lengsfield, B. D. Terris, and O. Hellwig, Appl. Phys. Lett. **95**, 262504 (2009).

[35] I. Tudosa, M. V. Lubarda, K. T. Chan, M. A. Escobar, V. Lomakin, and E. E. Fullerton, Appl. Phys. Lett. **100**, 102401 (2012).

[36] O. Hovorka, Y. Liu, K. A. Dahmen, and A. Berger, Appl. Phys. Lett. **95**, 192504 (2009); O. Hovorka, R. F. L. Evans, R. W. Chantrell, and A. Berger, *ibid.* **97**, 062504 (2010); O. Hovorka, J. Pressesky, G. Ju, A. Berger, and R. W. Chantrell, *ibid.* **101**, 182405 (2012).

[37] O. Hovorka, R. F. L. Evans, R. W. Chantrell, Y. Liu, K. A. Dahmen, and A. Berger, J. Appl. Phys. **108**, 123901 (2010).

[38] O. Hovorka, Y. Liu, K. A. Dahmen, and A. Berger, J. Magn. Magn. Mater. **322**, 459 (2010).

[39] A. D. Stoycheva and S. J. Singer, Phys. Rev. Lett. **84**, 4657 (2000).

[40] M. Seul and D. Andelman, Science **267**, 476 (1995), and references therein.

[41] G. Malescio and G. Pellicane, Nature **2**, 97 (2003).

[42] A. Hubert and R. Schäfer, *Magnetic Domains*, Chapters 3 and 5 (Springer-Verlag, Berlin, 1998).

[43] M. S. Pierce, J. E. Davies, J. J. Turner, K. Chesnel, E. E. Fullerton, J. Nam, R. Hailstone, S. D. Kevan, J. B. Kortright, K. Liu, L. B. Sorensen, B. R. York, and O. Hellwig, Phys. Rev. B **87**, 184428 (2013).

[44] M. S. Pierce, C. R. Buechler, L.B. Sorensen, S. D. Kevan, E. A. Jagla, J. M. Deutsch, T. Mai, O. Narayan, J. E. Davies, K. Liu, G. T. Zimanyi, H. G. Katzberger, O. Hellwig, E. E. Fullerton, P. Fischer, and J. B. Kortright, Phys. Rev. B **75**, 144406 (2007).

[45] O. Hellwig, G. P. Denbeaux, J. B. Kortright, and E. E. Fullerton, Physica B: Phys. Cond. Matter **336**, 136 (2003).

[46] M. A. Marioni, N. Pilet, T. V. Ashworth, R. C. O'Handley, and H. J. Hug, Phys. Rev. Lett. **97**, 027201 (2006).

[47] G. H. Wannier, Phys. Rev. **79**, 357 (1950); Phys. Rev. B **7**, 5017 (1973).

[48] R. M. F. Houtappel, Physica (Amsterdam) **16**, 391 (1950); **16**, 425 (1950).

[49] E. Mengotti, L. J. Heyderman, A. Bisig, A. Fraile Rodríguez, L. Le Guyader, F. Nolting, and H. B. Braun, J. Appl. Phys. **105**, 113113 (2009).

[50] N. Rougemaille, F. Montaigne, B. Canals, A. Duluard, D. Lacour, M. Hehn, R. Belkhou, O. Fruchart, S. El Moussaoui, A. Bendounan, and F. Maccherozzi, Phys. Rev. Lett. **106**, 057209 (2011).

[51] V. E. Kireev, R. S. Khymyn, B. A. Ivanov, and C. E. Zaspel, arXiv:1201.1747 (2012).

[52] K. Nielsch, R. B. Wehrspohn, J. Barthel, J. Kirschner, S. F. Fischer, H. Kronmuller, T. Schweinbock, D. Weiss, and U. Gosele, J. Magn. Magn. Mater. **249**, 234 (2002).

[53] Y. Shokef and T. C. Lubensky, Phys. Rev. Lett. **102**, 048303 (2009).

[54] Y. Matsui, K. Nishio, and H. Masuda, Small **2**, 522 (2006).

[55] G. Q. Ding, R. Yang, J. N. Ding, N. Y. Yuan, and Y. Y. Zhu, Nanoscale Res. Lett. **5**, 1257 (2010).

[56] O. Ozatay, T. Hauet, S. H. Florez, J. A. Katine, A. Moser, J.-U. Thiele, L. Folks, and B. D. Terris, Appl. Phys. Lett. **95**, 172502 (2009).

[57] Y. I. Dublenych, J. Phys.: Condens. Matter **25**, 406003 (2013).